
Article:
Bloomfield, M.E., Christofidou, K.A. orcid.org/0000-0002-8064-5874 and Jones, N.G. (2019) Effect of Co on the phase stability of CrMnFeCoxNi high entropy alloys following long-duration exposures at intermediate temperatures. Intermetallics, 114. ISSN 0966-9795

https://doi.org/10.1016/j.intermet.2019.106582

Effect of Co on the phase stability of $CrMnFeCo_xNi$ high entropy alloys following long-duration exposures at intermediate temperatures

M. E. Bloomfield, K. A. Christofidou, N. G. Jones*

Department of Materials Science and Metallurgy, University of Cambridge, 27 Charles Babbage Road, Cambridge, CB3 0FS, U.K.
* ngj22@cam.ac.uk; 0044122334367

Abstract

The effect of Co on the phase stability of the $CrMnFeCo_xNi$ family of alloys, where the atomic ratio x = 0, 0.5, 1.5, has been experimentally established following 1000 hour heat treatments at 700 and 900˚C and up to 5000 hours at 500˚C. All the alloys were single phase fcc in the homogenised condition, except for CrMnFeNi which also contained bcc precipitates that remained present following exposures at 900˚C and 700˚C. The exposures at 900˚C and 700˚C also resulted in the formation of σ phase precipitates in the CrMnFeNi and $CrMnFeCo_{0.5}Ni$ alloys but not in the $CrMnFeCo_{1.5}Ni$ alloy. These data, in conjunction with results previously published in the literature, conclusively establish that Co stabilises the fcc matrix at elevated temperatures. However, at 500˚C, further bulk decomposition in the CrMnFeNi alloy was observed and produced a fine-scale intergrowth of a NiMn $L1_0$ phase and CrFe σ phase. Grain boundary precipitates were also observed following exposure at 500˚C in the $CrMnFeCo_{0.5}Ni$ and $CrMnFeCo_{1.5}Ni$ alloys. Four different phases were observed on the grain boundaries of the $CrMnFeCo_{0.5}Ni$ alloy (Cr carbide, σ, FeCo B2 and NiMn $L1_0$), whilst only two phases were found on the grain boundaries of the $CrMnFeCo_{1.5}Ni$ alloy (Cr carbide and NiMn $L1_0$). The experimental observations facilitated an assessment of the fidelity of current thermodynamic predictions of phase equilibria. All the phases predicted were observed experimentally and the σ stability fitted the experimental observations well. However, at lower temperatures, thermodynamic predictions were less consistent with experimental observations, underpredicting the extent of the B2 phase field and failing to predict the formation of the $L1_0$ phase.

Key words: A. High-Entropy Alloys; B. Phase stability; C. Heat treatment; D. Microstructure; E. Phase stability, prediction; F. Electron microscopy

Introduction

Multi-principal-component alloys, which maximise configurational entropy, so-called High Entropy Alloys (HEAs), were defined by Yeh et al. as "Alloys with five or more principal elements each with a concentration between 5 and 35at.%" [1]. The most widely studied set of alloys following this approach are based on the 3d transition metals, of which Cr, Fe, Co and Ni are the most commonly used elements [2]. One such example is the equiatomic CrMnFeCoNi alloy, first reported by Cantor et al. in 2004 [3]. This quinary alloy has been shown to exhibit many useful properties including a high Hall-Petch coefficient [4,5] and a negative temperature dependence of strength and ductility [5,6], leading to enhanced fracture toughness at cryogenic temperatures [7]. However, the alloy has insufficient yield strength at room temperature for many engineering applications [8]. Furthermore, while it was originally thought to be stable as a single solid solution phase at all temperatures below the melting point, studies have revealed the precipitation of a topologically close packed (TCP) σ phase following heat treatments below 800˚C [9–11]. In addition, below 500˚C, three different precipitate phases formed, which were identified as NiMn $L1_0$, FeCo B2 and Cr-rich bcc [10].

The formation of σ phase in this temperature range is also observed in austenitic stainless steels [12] and Ni-base superalloys [13], where it has a highly deleterious effect on the mechanical properties of these materials. As such, these alloys are unsuitable for structural applications at elevated temperatures where the σ phase might be expected to form. Consequently, there has been interest in developing non-equiatomic alloys within the CrMnFeCoNi system that suppress σ formation and enhance mechanical properties [14–22]. However, effective design of new alloys in this system requires a complete understanding of the effect of composition and temperature on phase stability, particularly of the σ phase.

A key challenge in the development of HEAs arises from the vast compositional freedom inherent in multi-principal component systems, which makes systematic experimental investigation alone prohibitively time-consuming. As such, the use of computational methods to predict the phase stability across multi-dimensional compositional space is essential [23,24]. One such approach is the CALPHAD method [25], which has proven highly effective in more conventional alloy systems. However, the underpinning thermodynamic databases are predominantly based on the phase equilibria of binary and, to a lesser extent, ternary systems and an increasing body of evidence shows that the fidelity of

their predictions in higher order systems, particularly at near-equiatomic compositions, is unreliable [18,26–31]. Furthermore, many studies of phase stability in HEAs have focused on temperatures in excess of 1000˚C [18,28,30], where single-phase solid solutions are more likely to form due to the enhanced entropic contribution to Gibbs energy. Consequently, there is a particular lack of experimental data at lower temperatures and, as a result, many thermodynamic predictions at these temperatures remain unverified. Where experimental data does exist, it is often acquired from material that has not been subjected to an appropriate homogenisation heat treatment and subsequent thermal exposure to promote the precipitation of stable phases [31,32]. This is particularly true when investigating phase stability at low homologous temperatures, where there may be severe kinetic limitations to phase formation, as evidenced in recent radiotracer studies [33–35]. So far, comparisons of CALPHAD predictions, using the TCHEA1 database, with experimental results have shown that the calculations significantly underestimate the temperature range of stability of the σ phase [27–29].

In order to improve our understanding of phase stability in the CrMnFeCoNi system, it is necessary to determine the effect of each constituent element on the microstructural equilibrium. It has been well established that Cr is the main σ forming element in the CrMnFeCoNi system and as such promotes the formation of the σ phase [13,14,28,36–41]. In addition, systematic studies of the effect of Mn and Ni have recently been carried out, which assessed the phase stability following long-term exposures at temperatures between 500 and 900˚C [27,29]. This is the temperature range in which second phase precipitates have been observed in the equiatomic alloy [9,10]. The studies established that Mn promotes σ formation whereas Ni stabilises the fcc matrix. However, to date, similarly detailed studies have not been performed when varying Co or Fe and so the effect of these elements remains unclear. The role of Co is of particular interest due to its high cost relative to the other constituent elements, which could significantly undermine the commercial uptake of these alloys.

The first study of the Co-free CrMnFeNi alloy by Wu et al. [42] reported that other phases, in addition to the fcc phase, were present following homogenisation at 1100˚C for 24 h. Whilst no attempt was made to identify these phases, the associated XRD pattern contained reflections that are characteristic of the σ phase, along with others that might be consistent with a bcc phase. A further investigation of Co variations was carried out by Bracq et al. [28] who observed fcc, bcc and σ phases in the Co-free quaternary following a 144 h

exposure at 1000˚C. In contrast, the 1100˚C annealed specimen contained only an fcc and bcc phase, suggesting that the σ solvus may lie in the region 1000 - 1100˚C. Alloys containing 10 and 90 at.% Co, with other elements in equal amounts, were also investigated following 144 h heat treatments at 1100˚C. The alloy containing 10 at.% was single phase fcc whereas the 90 at.% Co alloy contained a second hcp Co phase with the same composition as the fcc matrix. This was attributed to an allotropic, martensitic transformation during cooling and hence, hcp Co was not considered an equilibrium phase at 1100˚C. The most comprehensive study to date on the effect of Co was carried out by Zhu et al. [19] on samples containing 5, 10 and 20 at.% Co, annealed at 850˚C for 48 h. The 5 at.% Co alloy contained dark and light precipitates which were together identified as the σ phase. The 10 at.% Co sample also contained σ precipitates, though in much smaller volume fraction and the 20 at.% Co alloy was single phase fcc.

Thus, the current literature data suggest that Co enhances the stability of the fcc solid solution relative to the σ phase in concentrations up to 20 at.%. However, this conclusion is based solely on results from exposures ≥ 850˚C, which may be above the solvus temperature of any intermetallic phases; and following relatively short exposures of 24 – 144 h, which may not yield equilibrium microstructures. Furthermore, in these studies [19,28,42], the specimens were heat-treated directly from the as-cast condition, which often contains solidification-induced microsegregation [29,32,43], as confirmed in the specimens investigated by Zhu et al. [19]. This segregation may influence the microstructural features subsequently formed, particularly at lower temperatures and following short exposures where limited diffusion can take place.

Therefore, to elucidate the role of Co on phase equilibria in the $CrMnFeCo_xNi$ system, this manuscript presents a systematic study of the phase equilibria of three alloys, where the atomic ratio was x = 0, 0.5, 1.5. All of the alloys were homogenised just below their solidus temperatures prior to long duration exposures of at least 1000 h at 500, 700 and 900˚C; the temperature range in which phase decomposition has been shown to occur in other alloys within the CrMnFeCoNi system [9,10,19,27].

Experimental

Three alloy compositions, CrMnFeNi, $CrMnFeCo_{0.5}Ni$ and $CrMnFeCo_{1.5}Ni$, which correspond to 0, 11.1 and 27.3 at.% Co respectively, were prepared by arc-melting elemental metals, of at least 99.5% purity, under an inert argon atmosphere. To improve the

macroscopic homogeneity of the materials, each ingot was inverted and re-melted a total of five times.

Differential Scanning Calorimetry (DSC) was performed on the as-cast alloys using a 'Netzsch DSC 404' calorimeter operated under flowing argon at temperatures between 50 - 1450˚C with a heating and cooling rate of 10˚C / min. The as-cast ingots were subsequently solution treated for 100 h at 1170˚C, ~50˚C below the lowest incipient melting point determined from the DSC data. To prevent oxidation during the homogenisation heat-treatment, each ingot was encapsulated within an evacuated and argon backfilled quartz ampoule. Transverse sections, approximately 10 mm thick, were taken from the homogenised and quenched ingots. These were re-encapsulated and subjected to long-duration (at least 1000 h) heat treatments at 500, 700 and 900˚C, followed by rapid water quenching.

Specimens were prepared for Scanning Electron Microscopy (SEM) analysis by conventional grinding and polishing routes. Each sample was subjected to rough and fine grinding using SiC paper followed by polishing using 6 and 3μm diamond suspensions. Final polishing was carried out using a 0.04μm colloidal silica solution. The specimens were characterised in each condition using back-scattered electron (BSE) imaging in a Zeiss Gemini 300 scanning electron microscope operated at 15kV. Energy dispersive X-ray (EDX) elemental partitioning maps and point compositions were also obtained from Kα peaks using an Oxford Instruments Symmetry detector. An average of at least ten EDX spectra points were used for the compositional quantification of each phase. Further characterisation of fine scale structures was carried out using an FEI Osiris scanning transition electron microscope (STEM) equipped with Super-X EDX detectors. TEM specimens were prepared from 3mm diameter discs, thinned by twin-jet electropolishing. Lamella containing specific areas of interest were also extracted from the bulk material by focussed ion beam (FIB) milling.

Additional phase characterisation was performed by X-ray diffraction (XRD) using Ni filtered Cu Kα radiation on a Bruker D8 Advance diffractometer equipped with a LYNXEYE-XE position sensitive detector. Diffraction data was acquired in the angular range of 20 - 125˚ 2θ whilst the sample was rotated to improve sampling statistics. Phase identification and lattice parameters were obtained by full-pattern refinements of the XRD data using the Pawley fitting procedure [44] in TOPAS-Academic.

Results

The bulk composition of each alloy was obtained from the homogenised condition by averaging five large area EDX maps. Each map was at least 500 × 500 µm and the quoted error is the standard deviation between the five measurements. In all cases, the individual elemental concentrations, displayed in Table 1, were within ± 1 at.% of their target composition. The melting temperatures of each alloy, in the homogenised condition, were obtained from DSC as the onset of melting and are displayed in Table 2.

$CrMnFeCo_{1.5}Ni$

The microstructure of the $CrMnFeCo_{1.5}Ni$ ($Co_{1.5}$) alloy was studied in the homogenised condition and following subsequent long-term heat treatments at 900, 700 and 500˚C. BSE images for each heat-treatment condition are displayed in Fig. 1. In each condition, the specimens had a large grained microstructure and BSE contrast appeared to reflect crystal orientation rather than compositional variations. Dark particles, present throughout each specimen, were identified as pores or oxide inclusions. The mottled contrast within the grains, which is particularly apparent at higher magnifications, is a polishing artefact attributed to chemical etching due to the alkaline nature of the colloidal silica polishing solution. In the specimens exposed at 900 and 700˚C, macroscopic chemical homogeneity was confirmed by EDX; a typical example of which is shown in the elemental partitioning maps, taken from the 700˚C specimen (dashed outline), shown at the bottom of Fig. 1. In contrast, following exposure at 500˚C, fine-scale discrete precipitates were occasionally observed on the grain boundaries. An exemplar BSE image of these precipitates is shown in Fig. 2, along with corresponding elemental partitioning maps. Whilst the precipitates were too small obtain reliable elemental quantification of their composition, the elemental partitioning maps revealed that they were enriched in NiMn and depleted in the other elements relative to the matrix.

X-ray diffraction patterns from each heat-treatment condition are shown in Fig. 3. All patterns contained only reflections that were consistent with a single fcc phase, with a measured lattice parameter of 3.59 Å. No reflections corresponding to the grain boundary precipitates in in the 500˚C specimen were observed, which is unsurprising considering their small size and volume fraction.

$CrMnFeCo_{0.5}Ni$

BSE images of the $CrMnFeCo_{0.5}Ni$ ($Co_{0.5}$) alloy following homogenisation and long duration exposures are shown in Fig. 4. As with the $Co_{1.5}$ alloy, homogenisation of the $Co_{0.5}$ alloy produced a single phase material, with no evidence of any elemental partitioning in the related EDX maps. Following 1000 h heat-treatment at 900˚C, a new light-contrast phase was observed to have precipitated along the grain boundaries and within the grains. The grain boundary precipitates were large and blocky, whilst the intragranular precipitates had an elongated lenticular morphology. EDX elemental partitioning maps, taken from within the dashed box, indicated that these precipitates were enriched in Cr, depleted in Ni and Mn and had similar levels of Co and Fe when compared to the surrounding matrix.

Following long duration exposure at 700˚C, similar light-contrast precipitates are observed along the grain boundaries along with some dark-contrast precipitates. These two phases were generally observed on separate grain boundaries, although they did also appear coincidently at certain locations, as shown in the higher magnification image in Fig. 4. EDX elemental partitioning maps obtained from within the dashed region of the image are shown below. These maps indicate that both precipitate phases are enriched in Cr, but they exhibit marked differences in the partitioning of the other elements. The light-contrast phase was depleted in both Mn and Ni when compared to the surrounding matrix material and a slight depletion in Fe was also noted, whilst the Co concentration appeared to be very similar to the matrix. Conversely, the dark-contrast precipitates were depleted in all elements relative to the matrix, with the exception of Cr, in which it was more enriched than the light-contrast phase.

On initial inspection, the material exposed at 500˚C did not appear contain any second phases. However, higher magnification images revealed very fine-scale light and dark precipitates at discrete locations on the grain boundaries. These precipitates were too fine to resolve in SEM-based EDX elemental segregation maps, but their appearance in BSE was very similar to the phases observed in the 700˚C condition.

The XRD patterns corresponding to the homogenised and long duration exposed conditions of the $Co_{0.5}$ alloy are displayed in Fig. 5. As with the $Co_{1.5}$ alloy, each pattern contained strong reflections corresponding to an fcc phase with a lattice parameter of 3.61 Å, likely to be the matrix. Initially, no additional reflections were observed corresponding to the

precipitate phases observed in the microstructure. This is unsurprising as considering the relatively large grain sizes in these alloys, the overall volume fraction of precipitate phases will be small. However, further sampling of the 900˚C specimen did reveal additional reflections between 42 and 45 ˚2θ, see insert in Fig. 5. These peaks are often reported as being characteristic of the σ phase [19,27,28,45,46], and therefore, it is thought that the light-contrast precipitates correspond to the σ phase.

Individual phase compositions, obtained by averaging ten or more point EDX spectra from each phase, are provided in Table 3. As with the bulk compositions, the quoted error is the standard deviation of the individual measurements. The composition of the fcc matrix in each condition was found to be within 1 at.% of the bulk composition, emphasising the small volume fraction of precipitates present. Notably, the composition of the light-contrast phase was highly consistent between the 900 and 700˚C conditions, with a composition of approximately 45Cr-15Mn-20Fe-11Co-9Ni (at.%). This is in good agreement with the composition of the σ phase reported by several other studies investigating alloys derived from the CrMnFeCoNi system [9,10,29]; and with the σ phase field in the Cr-Mn-Fe ternary phase diagram at 700˚C [47], supporting the identification of σ reflections in the diffraction data above. Due to their small size, compositional analysis of the dark-contrast precipitates was much more challenging and, as such, there were more substantial errors associated with the elemental quantification. However, as was evident in the elemental partitioning maps shown in Fig. 4, the quantified results indicated that these precipitates had a substantially higher Cr-content and significantly lower Fe- and Co- contents than the σ phase. Similar backscattered image contrast and elemental partitioning trends of a grain boundary phase have been reported previously in other thermally exposed CrMnFeCoNi alloys which were shown to be the $M_{23}C_6$ carbide phase [9,29]. Therefore, whilst no confirmatory crystallographic data has been acquired, it is believed that these precipitates are likely to be a carbide phase formed as a result of an unintentional incorporation of C.

CrMnFeNi

BSE images and corresponding EDX elemental partitioning maps for the CrMnFeNi alloy are displayed in Fig. 6. The homogenised specimen consisted of a large grained microstructure which contained annealing twins. Large, faceted precipitates were observed both at the grain boundaries and within the matrix grains, particularly along twin boundaries. EDX elemental

partitioning maps revealed that these precipitates were rich in Cr, depleted in Mn & Ni and had a similar concentration of Fe relative to the matrix. The corresponding X-ray diffraction pattern, shown in Fig. 7, revealed two distinct sets of reflections that were indexed to an fcc and a bcc phase, with lattice parameters 3.62 and 2.87 Å respectively. The multi-component solid solution phases in the CrMnFeCoNi system are known to adopt an fcc structure, whilst the composition of the Cr-rich phase, given in Table 4, was consistent with the large bcc phase field within the Cr-Mn-Fe ternary phase diagram at 1200˚C [48]. This two-phase microstructure was consistent with the DSC trace shown in Fig. 8, which featured two melting events.

Thermal exposure of the homogenised material at 900˚C resulted in extensive precipitation of a light-contrast phase which formed near-continuous layers along some matrix grain boundaries. Widespread formation of small, dark-contrast lath-shaped and spheroidal precipitates were observed throughout the material. The spheroidal precipitates often contained secondary lath-shaped precipitates of a lighter-contrast. Representative elemental partitioning maps of a grain boundary region in the 900˚C specimen indicated that all the precipitate phases were Cr-rich when compared to the matrix. Additionally, all the precipitates were depleted in both Mn and Ni relative to the matrix. However, the Fe partitioning varied between the light and dark precipitates. The Fe-content of the dark-contrast precipitates was depleted with respect to the matrix, whereas, the light-contrast phase had a similar Fe concentration to the matrix. Furthermore, the lath-shaped secondary precipitates within the dark-contrast spheroidal particles had the same elemental partitioning behaviour as the matrix. As such, three distinct phases were observed within the microstructure and their quantified phase compositions are provided in Table 4. The matrix phase was substantially depleted of Cr and enriched in Ni and Mn, reflecting the large volume fraction of precipitates. The composition of the light-contrast phase was around 44Cr-19Mn-26Fe-11Ni (at.%) which is consistent with the σ phase that was identified in the $Co_{0.5}$ specimens exposed at 900 and 700˚C. The dark-contrast precipitates however, contained ~ 64 at.% Cr and their composition was consistent with the bcc phase in the Cr-Mn-Fe ternary phase diagram at 900˚C [48]. Phase identification was further supported by the corresponding XRD pattern, displayed in Fig. 7, which contained reflections consistent with an fcc (a = 3.62 Å), bcc (a = 2.88 Å) and σ phase (a = 8.83 Å, b = 4.57 Å). The presence of spherical bcc particles containing secondary precipitates suggests that they are remnants of the bcc particles formerly present in the homogenised condition.

Following long duration exposure at 700˚C, the Co-free quaternary contained dark- and light-contrast precipitates, very similar to those observed at 900˚C. As such, these dark and light phases are assumed to be the bcc and σ phases respectively. As in the 900˚C condition, lath-shaped bcc precipitates appeared throughout the microstructure, though they were generally finer. Conversely, the former bcc particles were larger but had internally decomposed yielding finer secondary precipitates. There also appeared to be a much smaller volume fraction of σ phase which was only observed on grain boundaries, predominantly coincident with the Cr-rich former bcc precipitates. Representative EDX data from the 700˚C condition showed that the dark- and light-contrast precipitates had the same elemental partitioning trends as in the 900˚C exposed condition. However, the corresponding X-ray diffraction pattern, shown in Fig. 7, only contained reflections consistent with the presence of an fcc and a bcc phase, which had the same lattice parameters as in the 900˚C specimen. No reflections corresponding to the σ phase were observed which, again, suggests a decrease in the volume fraction of σ compared to the 900˚C exposed condition.

The microstructure of the material exposed for 1000 h at 500˚C, shown in Fig. 6, initially appeared similar to the homogenised condition, containing large dark-contrast particles within a lighter matrix. However, higher magnification imaging revealed that both the matrix and former bcc precipitates had decomposed to form complex multi-phase nanocrystalline structures. A BSE image of a former bcc precipitate and the surrounding matrix, Fig. 9a, shows that the former matrix consisted of a convoluted inter-growth of light and dark phases, with colonies of lamellar of varying interlamellar spacing. The former bcc precipitate, which had a darker overall contrast, contained a finer convolution of dark and light phases. A higher magnification image of the boundary between a former bcc precipitate and the former matrix is shown in Fig. 9b; EDX elemental partitioning maps, (i) through (iv), correspond to the dashed region. In this region, a significant coarsening of the microstructure at the former grain boundary allowed for a closer examination of the phases present. In the former matrix region, at the bottom of the image, dark-contrast particles featuring annealing twins were surrounded by a near-continuous light-contrast phase. However, in the former bcc precipitate region, at the top of the image, the phases were too fine to resolve in SEM. Elemental partitioning maps, corresponding to the dashed area of the image, showed that the former bcc region remained Cr-rich and depleted of Mn and Ni compared with the former matrix. The Fe-content of each region appeared to be similar, though there was significant partitioning of

Fe to the former grain boundaries. Determining the elemental partitioning behaviour of the fine microstructures within each region was beyond the resolution of SEM-based EDX except for at the former grain boundary, in Fig. 9b, where a coarsening of the microstructure revealed a continuous light-contrast CrFe-rich phase; and discrete, dark-contrast NiMn-rich particles.

In order to further characterise the phases present in this alloy, TEM microanalysis was employed. The STEM image and corresponding EDX elemental partitioning maps of the lamellar region revealed that the light and dark contrast phases were CrFe and NiMn-rich respectively.

The XRD pattern for the 500˚C condition, shown in Fig. 7, includes reflections corresponding to an fcc (a = 3.61 Å), bcc (a = 2.88 Å) and σ phase (a = 8.78 Å, c = 4.56 Å), which were also present in the 900˚C condition. Additional reflections were also observed which correspond to a new ordered $L1_0$ phase with lattice parameters a = 2.63 Å and c = 3.52 Å. The relative intensity of the reflections from each phase indicate that the volume fraction of the fcc and bcc phases has decreased substantially, so that the $L1_0$ and σ phases are now the majority phases. This suggests that the light- and dark-contrast phases observed correspond to the CrFe-rich σ phase and the NiMn-based $L1_0$ phase respectively.

STEM-based EDX phase quantifications, displayed in Table 4, were obtained from the EDX data in Fig. 10, based on an average of five area spectra within each lamella. It was found that the CrFe-rich σ phase contained around 10 at.% Mn and 6 at.% Ni with the compositional balance equally split between Cr and Fe. Conversely, the NiMn-based $L1_0$ phase contained less than 5 at.% of Cr and Fe with the balance composed of Ni and Mn in an approximately equiatomic ratio. It should be noted that, due to the small precipitate size, the EDX signal measured for one precipitate may include signal from adjacent phases.

Discussion

Effect of Co on phase stability

Based on the data presented above, and previous results published in the literature [9,10,28], the influence of Co on the phase stability of $CrMnFeCo_xNi$ alloys can be clearly established. It is evident that Co is a strong fcc solid solution stabilising element at elevated temperatures, which corresponds well with the trends expected from electronic structure calculations, such

as average d-orbital energy levels or valence electron concentrations [49,50,51]. This is most clearly demonstrated by the presence of an fcc + bcc two-phase field below the solidus in the Co-free quaternary. The formation of a bcc phase in this alloy has been previously reported by Bracq et al. [28] in specimens exposed at 1100˚C. Raising the Co-content to an atomic fraction 0.5, or beyond, increased the relative stability of the fcc solid solution phase, which resulted in a single-phase fcc region below the solidus. This single-phase field expands as a function of increasing Co concentration, depressing the formation of the σ phase to lower temperatures. For example, in the present study, σ phase precipitates were observed at 900˚C and below in the Co-free and $Co_{0.5}$ specimens; but were not present in any of the heat-treated $Co_{1.5}$ specimens. This trend fits well with previous studies of the equiatomic CrMnFeCoNi alloy which have shown that the σ phase is stable at 700˚C but not at 900˚C [9,10].

A more precise determination of the σ phase solvus was attempted using the DSC data, displayed in Fig. 8, which was obtained on heating for each condition. A thermal event, believed to correspond to the σ solvus, was observed only in the CrMnFeNi quaternary specimens exposed at 700˚C and 500˚C. This is unsurprising as these were the samples that appeared to have the greatest volume fraction of σ phase. The apparent σ solvus, between 1040 and 1090˚C, is also in good agreement with the work of Bracq et al. [28], who observed σ at 1000˚C but not at 1100˚C. The DSC trace for the 500˚C quaternary specimen also contained a separate, much larger, thermal event between 650-750˚C; this is believed to correspond to the solvus of the $L1_0$ phase.

Formation of intermetallic phases at low temperatures

The potential for the formation of intermetallic phases increases at low temperatures, as the contribution of entropy to the Gibbs energy is diminished. This is reflected in the microstructures of the alloys exposed at 500˚C. At this temperature, the Co-free quaternary alloy underwent bulk decomposition, forming a fine scale intergrowth of the ordered NiMn $L1_0$ phase and σ phase. Similarly, fine precipitates, thought to be the σ phase, were present on the grain boundaries of the $Co_{0.5}$ alloy, whilst the $Co_{1.5}$ specimen contained NiMn-rich grain boundary precipitates. Based on the identification of a NiMn $L1_0$ phase in the Co-free quaternary, it may be assumed that the NiMn-rich phase in the $Co_{1.5}$ alloy also takes the $L1_0$ crystal structure. However, following a much longer exposure of 12000 h, Otto et al. [10] observed a FeCo B2 and a Cr-rich bcc phase, in addition to the NiMn $L1_0$ phase, on the grain

boundary of the equiatomic CrMnFeCoNi alloy. Their observation indicates that the formation of additional thermodynamically stable phases may be kinetically inhibited within 1000 h at 500˚C. Therefore, to establish whether the formation of additional phases was kinetically inhibited in the specimens heat-treated at 500˚C, samples of all three alloys were subjected to further exposures at 500˚C to achieve total exposure durations of 2500 and 5000 h.

Following these further exposures at 500˚C, additional fine-scale precipitates were clearly present on the grain boundaries of the $Co_{1.5}$ and $Co_{0.5}$ alloys, whilst no changes in phase constitution were observed in the Co-free alloy. BSE images and EDX elemental partitioning maps of representative grain boundary regions of the $Co_{1.5}$ alloy following these exposures are displayed in Fig. 11. The elemental partitioning maps revealed the presence of a Ni- and Mn- rich phase, as well as a Cr-rich phase. Both precipitates were depleted of all other elements relative to the matrix. Based on the phases previously identified in this system, the NiMn-rich precipitates are believed to be the $L1_0$ phase, whilst the Cr-rich phase is believed to be a carbide. This is supported by the observed C enrichment coincident with the Cr-rich precipitates in the elemental partitioning maps of the 5000 h condition. A slight enrichment of Fe and Co was also observed in the regions adjacent to the NiMn- and Cr-rich precipitates. However, there was no clear evidence within the data collected to suggest that these regions constituted an additional phase.

BSE images of typical grain boundary regions from the $Co_{0.5}$ alloy following further exposures along with elemental partitioning maps are shown in Fig. 12. From these data four different precipitate phases were identified. As in the 1000 h condition, there was evidence of dark- and light- contrast precipitates on the grain boundaries in the BSE image. These were both found to be Cr-rich but exhibited marked differences in the partitioning of the other elements. The dark contrast precipitates were depleted in all other elements, whereas, the light contrast precipitates were depleted in Ni and Mn but contained a similar concentration of Co and Fe to the surrounding matrix. As such, these precipitates are believed to be a Cr carbide phase and σ phase respectively. Other precipitates were found to be Ni- and Mn- rich, indicating that, at 500˚C, the $L1_0$ phase forms in all of the studied alloys. Evidence of precipitates enriched in both Fe and Co was also found, which, critically, also showed depletions in the concentrations of other elements. As such, these precipitates are believed to be the FeCo B2 phase which has been identified previously in the CrMnFeCoNi alloy [10].

The prolonged exposure times required to form certain precipitate phases at 500˚C means that care must be taken to distinguish between kinetic and thermodynamic influences on the observed phases at this temperature. Recent radiotracer [33–35] and inter-diffusion [52] studies have measured the individual diffusivities of each component element in the CrMnFeCoNi alloy and its constituent quaternaries. These data have highlighted that, within this system, the homologous temperature has a dominant influence on the diffusional kinetics. Thus, as the melting temperature of the alloys studied here increased with Co-content (Table 2), the diffusivities of each elemental species at a given temperature would be expected to decrease [53]. As such, the kinetics of phase formation may be slower in alloys with greater Co-contents, thereby enhancing the metastability of the fcc solid solution. However, to date, no appropriate diffusional data exists for the Co-free quaternary nor other related non-equiatomic alloys to conclusively establish and quantify the effect of Co on the kinetics of diffusion.

Fidelity of thermodynamic predictions

A predicted pseudo-binary phase diagram between CrMnFeNi and Co, calculated using the TCHEA3 database and ThermoCalc, is displayed in Fig. 13. The solidus is predicted to increase steadily with increasing Co-content and closely matches the values measured by DSC, to within 15˚C (Table 2). The phase diagram suggests that above ~4 at.% Co, a single fcc phase field exists below the solidus, whereas, with lower Co concentrations a bcc phase also forms during solidification. The extent of the fcc + bcc phase field is small and exists only to ~1050˚C. Below this temperature a large fcc + σ phase field is predicted, suggesting that the formation of the intermetallic phase is preferable to the bcc phase. The σ formation temperature decreases in a linear fashion with increasing Co concentration.

The experimental observations from this study, and previous studies [9,10] of the equiatomic quinary alloy, involving exposures of at least 1000 h, are indicated on the pseudo-binary phase diagram. Conditions that produced single-phase fcc microstructures are denoted with green squares, whilst those which contained σ phase precipitates are shown by red circles. Exposures that produced both σ and bcc precipitates are identified by purple hexagons and those for which produced other phases, including the $L1_0$, were present are represented by blue diamonds.

Comparing the TCHEA3 predictions with the experimentally observed phases shows that the trend of the predicted σ solvus fits well with the experimental data for alloys containing up to 20 at.% Co. However, when the Co-content was increased to an atomic ratio of 1.5, the absence of the σ phase at 700˚C suggests that increasing Co-content beyond the equiatomic concentration supresses the formation of σ substantially more than the linear trend predicted. The bcc phase observed in the Co-free quaternary was predicted by TCHEA3, but only at high temperatures. However, our experimental observations indicated that the bcc phase remained stable down to a temperature of at least 700˚C. There was also evidence of the bcc phase in the XRD pattern from the 500˚C specimen (Fig. 7), but due to the slow diffusion kinetics this phase could well be metastable. In addition, a Cr-based bcc phase was observed by Otto et al. [10] in CrMnFeCoNi at 500˚C, this reappearance of a bcc phase at higher Co-contents is not predicted by TCHEA3. However, a CoFe-based B2 phase was predicted at 500˚C in alloys containing ≥ 25 at.% Co. This phase was experimentally observed at 500˚C in the equiatomic quinary alloy [10] and in the $Co_{0.5}$ alloy studied here. Interestingly, definitive evidence of the B2 phase was not found in the $Co_{1.5}$ alloy, even after a 5000 h exposure. Again, the lack of clear experimental evidence of this phase in the $Co_{1.5}$ alloy may be due to kinetic suppression rather than thermodynamic stability. Nevertheless, the appearance of the B2 phase in the equiatomic and $Co_{0.5}$ alloys require an adjustment of the database to extend the compositional range of this phase to lower Co-contents at 500˚C.
A more major discrepancy between experimental results and thermodynamic predictions related to the formation of the ordered $L1_0$ intermetallic phase, which has been experimentally observed at 500˚C in all of the alloys within the considered compositional range. This phase was not predicted to form at all when the TCHEA3 database was used, despite being present in the MnNi [54], CoMnNi [55], CrMnNi [55] and FeMnNi [56] phase diagrams, which highlights an issue with the relative position of the corresponding Gibbs free energy curves.

Conclusions

This study has experimentally investigated the effect of Co concentration on phase stability in the $CrMnFeCo_xNi$ family of alloys and assessed the fidelity of equilibrium phase predictions of the latest High Entropy Alloy thermodynamic database.

The results show that Co effectively stabilises the fcc phase at elevated temperatures, suppressing the formation of the bcc and σ phases. In the homogenised condition, the Co-free quaternary contained bcc precipitates, while alloys containing ≥ 11.1 at.% Co were single phase fcc. Subsequent exposures at 900 and 700˚C resulted in the formation of σ phase precipitates in the Co-free and $Co_{0.5}$ specimens, but not in the $Co_{1.5}$ alloy, which remained single phase fcc. At 500˚C, the CrMnFeNi alloy underwent bulk fine-scale decomposition producing an intergrowth of a NiMn $L1_0$ and CrFe σ phase. Fine-scale precipitates were also observed on the grain boundaries of $Co_{0.5}$ and $Co_{1.5}$ alloys at this temperature. Four different precipitate phases, a Cr carbide, σ, an FeCo B2 and a NiMn $L1_0$ were observed on the grain boundaries of the $Co_{0.5}$ alloy, whilst only a Cr carbide and a NiMn $L1_0$ were found on the grain boundaries of the $Co_{1.5}$ alloy.

Thermodynamic predictions for this system described σ stability reasonably well but underestimated the stability of the bcc phase, which was experimentally observed at much lower temperatures than predicted. Moreover, they underpredicted the extent of the B2 phase field and failed to predict the formation of the ordered $L1_0$ phase at 500˚C. This portrays a general decrease in the fidelity of thermodynamic predictions at lower temperatures which may be attributed to the lack of appropriate low temperature experimental data in the literature. Consequently, at present, care should be taken when using thermodynamic models to predict low temperature phase stability in alloys of the CrMnFeCoNi system.

Acknowledgements

The authors would like to thank S. Rhodes and G. Divitini for their assistance and H.T. Pang for helpful discussions. The authors acknowledge support from the Rolls-Royce / EPSRC Strategic Partnership [grant number EP/M005607/1]. The underlying data from this work can be found in the University of Cambridge data repository: https://doi.org/10.17863/CAM.41630.

References

[1] M.-H. Tsai, J.-W. Yeh, High-Entropy Alloys: A Critical Review, Mater. Res. Lett. 2 (2014) 107–123. doi:10.1080/21663831.2014.912690.

[2] D.B. Miracle, O.N. Senkov, A critical review of high entropy alloys and related concepts, Acta Mater. 122 (2017) 448–511. doi:10.1016/j.actamat.2016.08.081.

[3] B. Cantor, I.T.H. Chang, P. Knight, A.J.B. Vincent, Microstructural development in equiatomic multicomponent alloys, Mater. Sci. Eng. A. 375–377 (2004) 213–218. doi:10.1016/J.MSEA.2003.10.257.

[4] W.H. Liu, Y. Wu, J.Y. He, T.G. Nieh, Z.P. Lu, Grain growth and the Hall–Petch relationship in a high-entropy FeCrNiCoMn alloy, Scr. Mater. 68 (2013) 526–529. doi:10.1016/J.SCRIPTAMAT.2012.12.002.

[5] F. Otto, A. Dlouhý, C. Somsen, H. Bei, G. Eggeler, E.P.P. George, The influences of temperature and microstructure on the tensile properties of a CoCrFeMnNi high-entropy alloy, Acta Mater. 61 (2013) 5743–5755. doi:10.1016/j.actamat.2013.06.018.

[6] A. Gali, E.P. George, Tensile properties of high- and medium-entropy alloys, Intermetallics. 39 (2013) 74–78. doi:10.1016/j.intermet.2013.03.018.

[7] B. Gludovatz, A. Hohenwarter, D. Catoor, E.H. Chang, E.P. George, R.O. Ritchie, A fracture-resistant high-entropy alloy for cryogenic applications, Science (80-.). 345 (2014) 1153–1158. doi:10.1126/science.1254581.

[8] W.H. Liu, T. Yang, C.T. Liu, Precipitation hardening in CoCrFeNi-based high entropy alloys, Mater. Chem. Phys. 210 (2018) 2–11. doi:10.1016/j.matchemphys.2017.07.037.

[9] E.J. Pickering, R. Muñoz-Moreno, H.J. Stone, N.G. Jones, Precipitation in the equiatomic high-entropy alloy CrMnFeCoNi, Scr. Mater. 113 (2016) 106–109. doi:10.1016/j.scriptamat.2015.10.025.

[10] F. Otto, A. Dlouhý, K.G. Pradeep, M. Kuběnová, D. Raabe, G. Eggeler, E.P. George,

Decomposition of the single-phase high-entropy alloy CrMnFeCoNi after prolonged anneals at intermediate temperatures, Acta Mater. 112 (2016) 40–52. doi:10.1016/j.actamat.2016.04.005.

[11] N.D. Stepanov, D.G. Shaysultanov, M.S. Ozerov, S. V. Zherebtsov, G.A. Salishchev, Second phase formation in the CoCrFeNiMn high entropy alloy after recrystallization annealing, Mater. Lett. 185 (2016) 1–4. doi:10.1016/j.matlet.2016.08.088.

[12] C.-C. Hsieh, W. Wu, Overview of Intermetallic Sigma () Phase Precipitation in Stainless Steels, ISRN Metall. 2012 (2012) 1–16. doi:10.5402/2012/732471.

[13] A.S. Wilson, Formation and effect of topologically close-packed phases in nickel-base superalloys, Mater. Sci. Technol. 33 (2017) 1108–1118. doi:10.1080/02670836.2016.1187335.

[14] A.J. Zaddach, R.O. Scattergood, C.C. Koch, Tensile properties of low-stacking fault energy high-entropy alloys, Mater. Sci. Eng. A. 636 (2015) 373–378. doi:10.1016/J.MSEA.2015.03.109.

[15] Z. Li, K.G. Pradeep, Y. Deng, D. Raabe, C.C. Tasan, Metastable high-entropy dual-phase alloys overcome the strength-ductility trade-off, Nature. 534 (2016) 227–230. doi:10.1038/nature17981.

[16] K.G. Pradeep, C.C. Tasan, M.J. Yao, Y. Deng, H. Springer, D. Raabe, Non-equiatomic high entropy alloys: Approach towards rapid alloy screening and property-oriented design, Mater. Sci. Eng. A. 648 (2015) 183–192. doi:10.1016/j.msea.2015.09.010.

[17] C.C. Tasan, Y. Deng, K.G. Pradeep, M.J. Yao, H. Springer, D. Raabe, Composition Dependence of Phase Stability, Deformation Mechanisms, and Mechanical Properties of the CoCrFeMnNi High-Entropy Alloy System, JOM. 66 (2014) 1993–2001. doi:10.1007/s11837-014-1133-6.

[18] D. Ma, M. Yao, K.G. Pradeep, C.C. Tasan, H. Springer, D. Raabe, Phase stability of non-equiatomic CoCrFeMnNi high entropy alloys, Acta Mater. 98 (2015) 288–296. doi:10.1016/j.actamat.2015.07.030.

[19] Z.G. Zhu, K.H. Ma, X. Yang, C.H. Shek, Annealing effect on the phase stability and mechanical properties of (FeNiCrMn) (100−x) Co x high entropy alloys, J. Alloys Compd. 695 (2017) 2945–2950. doi:10.1016/j.jallcom.2016.11.376.

[20] P. Wilson, R. Field, M. Kaufman, The use of diffusion multiples to examine the compositional dependence of phase stability and hardness of the Co-Cr-Fe-Mn-Ni high entropy alloy system, Intermetallics. 75 (2016) 15–24. doi:10.1016/j.intermet.2016.04.007.

[21] A. Kauffmann, M. Stüber, H. Leiste, S. Ulrich, S. Schlabach, D.V. Szabó, S. Seils, B. Gorr, H. Chen, H.-J. Seifert, M. Heilmaier, Combinatorial exploration of the High Entropy Alloy System Co-Cr-Fe-Mn-Ni, Surf. Coatings Technol. 325 (2017) 174–180. doi:10.1016/j.surfcoat.2017.06.041.

[22] K. Ming, X. Bi, J. Wang, Microstructures and deformation mechanisms of Cr26Mn20Fe20Co20Ni14 alloys, Mater. Charact. 134 (2017) 194–201. doi:10.1016/J.MATCHAR.2017.10.022.

[23] D. Miracle, B. Majumdar, K. Wertz, S. Gorsse, New strategies and tests to accelerate discovery and development of multi-principal element structural alloys, Scr. Mater. 127 (2017) 195–200. doi:10.1016/J.SCRIPTAMAT.2016.08.001.

[24] F. Tancret, I. Toda-Caraballo, E. Menou, P.E.J. Rivera Díaz-Del-Castillo, Designing high entropy alloys employing thermodynamics and Gaussian process statistical analysis, Mater. Des. 115 (2017) 486–497. doi:10.1016/J.MATDES.2016.11.049.

[25] N. (Nigel) Saunders, N. Saunders, CALPHAD : calculation of phase diagrams : a comprehensive guide / by N. Saunders and A.P. Miodownik., Pergamon, London, 1998.

[26] K. Guruvidyathri, K.C. Hari Kumar, J.W. Yeh, B.S. Murty, Topologically Close-packed Phase Formation in High Entropy Alloys: A Review of Calphad and Experimental Results, JOM. 69 (2017) 2113–2124. doi:10.1007/s11837-017-2566-5.

[27] K.A. Christofidou, T.P. McAuliffe, P.M. Mignanelli, H.J. Stone, N.G. Jones, On the prediction and the formation of the sigma phase in CrMnCoFeNi x high entropy alloys, J. Alloys Compd. 770 (2018) 285–293. doi:10.1016/j.jallcom.2018.08.032.

[28] G. Bracq, M. Laurent-Brocq, L. Perrière, R. Pirès, J.-M. Joubert, I. Guillot, The fcc solid solution stability in the Co-Cr-Fe-Mn-Ni multi-component system, Acta Mater. 128 (2017) 327–336. doi:10.1016/j.actamat.2017.02.017.

[29] K.A. Christofidou, E.J. Pickering, P. Orsatti, P.M. Mignanelli, T.J.A. Slater, H.J. Stone, N.G. Jones, On the influence of Mn on the phase stability of the CrMn x FeCoNi high entropy alloys, Intermetallics. 92 (2018) 84–92. doi:10.1016/j.intermet.2017.09.011.

[30] O.N. Senkov, S. V. Senkova, C. Woodward, D.B. Miracle, Low-density, refractory multi-principal element alloys of the Cr-Nb-Ti-V-Zr system: Microstructure and phase analysis, Acta Mater. 61 (2013) 1545–1557. doi:10.1016/j.actamat.2012.11.032.

[31] F. Zhang, C. Zhang, S.L. Chen, J. Zhu, W.S. Cao, U.R. Kattner, An understanding of high entropy alloys from phase diagram calculations, Calphad. 45 (2014) 1–10.

doi:10.1016/J.CALPHAD.2013.10.006.

[32] E.J. Pickering, N.G. Jones, High-entropy alloys: a critical assessment of their founding principles and future prospects, Int. Mater. Rev. 61 (2016) 183–202. doi:10.1080/09506608.2016.1180020.

[33] M. Vaidya, K.G. Pradeep, B.S. Murty, G. Wilde, S.V. Divinski, Bulk tracer diffusion in CoCrFeNi and CoCrFeMnNi high entropy alloys, Acta Mater. 146 (2018) 211–224. doi:10.1016/J.ACTAMAT.2017.12.052.

[34] M. Vaidya, K.G. Pradeep, B.S. Murty, G. Wilde, S. V. Divinski, Radioactive isotopes reveal a non sluggish kinetics of grain boundary diffusion in high entropy alloys, Sci. Rep. 7 (2017) 12293. doi:10.1038/s41598-017-12551-9.

[35] M. Vaidya, S. Trubel, B.S. Murty, G. Wilde, S.V. Divinski, Ni tracer diffusion in CoCrFeNi and CoCrFeMnNi high entropy alloys, J. Alloys Compd. 688 (2016) 994–1001. doi:10.1016/J.JALLCOM.2016.07.239.

[36] J.-M. Joubert, Crystal chemistry and Calphad modeling of the sigma phase, Prog. Mater. Sci. 22 (2008) 99–131. doi:10.1016/S0733-8619(03)00096-3.

[37] K. Ming, X. Bi, J. Wang, Microstructures and deformation mechanisms of Cr26Mn20Fe20Co20Ni14 alloys, Mater. Charact. 134 (2017) 194–201. doi:10.1016/J.MATCHAR.2017.10.022.

[38] J. Moon, Y. Qi, E. Tabachnikova, Y. Estrin, W.-M. Choi, S.-H. Joo, B.-J. Lee, A. Podolskiy, M. Tikhonovsky, H.S. Kim, Deformation-induced phase transformation of Co20Cr26Fe20Mn20Ni14 high-entropy alloy during high-pressure torsion at 77 K, Mater. Lett. 202 (2017) 86–88. doi:10.1016/J.MATLET.2017.05.065.

[39] M.-H. Tsai, K.-Y. Tsai, C.-W. Tsai, C. Lee, C.-C. Juan, J.-W. Yeh, Criterion for Sigma Phase Formation in Cr- and V-Containing High-Entropy Alloys, Mater. Res. Lett. 1 (2013) 207–212. doi:10.1080/21663831.2013.831382.

[40] M.-H. Tsai, K.-C. Chang, J.-H. Li, R.-C. Tsai, A.-H. Cheng, A second criterion for sigma phase formation in high-entropy alloys, Mater. Res. Lett. 4 (2016) 90–95. doi:10.1080/21663831.2015.1121168.

[41] N.D. Stepanov, D.G. Shaysultanov, M.A. Tikhonovsky, G.A. Salishchev, Tensile properties of the Cr-Fe-Ni-Mn non-equiatomic multicomponent alloys with different Cr contents, Mater. Des. 87 (2015) 60–65. doi:10.1016/j.matdes.2015.08.007.

[42] Z. Wu, H. Bei, F. Otto, G.M. Pharr, E.P. George, Recovery, recrystallization, grain growth and phase stability of a family of FCC-structured multi-component equiatomic solid solution alloys, Intermetallics. 46 (2014) 131–140.

doi:10.1016/j.intermet.2013.10.024.

[43] J.E. Saal, I.S. Berglund, J.T. Sebastian, P.K. Liaw, G.B. Olson, Equilibrium high entropy alloy phase stability from experiments and thermodynamic modeling, Scr. Mater. 146 (2018) 5–8. doi:10.1016/j.scriptamat.2017.10.027.

[44] G.S. Pawley, Unit-cell refinement from powder diffraction scans, J. Appl. Crystallogr. 14 (1981) 357–361. doi:10.1107/S0021889881009618.

[45] G. Laplanche, S. Berglund, C. Reinhart, A. Kostka, F. Fox, E.P. George, Phase stability and kinetics of σ-phase precipitation in CrMnFeCoNi high-entropy alloys, Acta Mater. 161 (2018) 338–351. doi:10.1016/J.ACTAMAT.2018.09.040.

[46] N.D. Stepanov, D.G. Shaysultanov, G.A. Salishchev, M.A. Tikhonovsky, E.E. Oleynik, A.S. Tortika, O.N. Senkov, Effect of v content on microstructure and mechanical properties of the CoCrFeMnNiVx high entropy alloys, J. Alloys Compd. 628 (2015) 170–185. doi:10.1016/j.jallcom.2014.12.157.

[47] K. Fritscher, H. Hammelrath, New ternary phase in Cr-Fe-Mn alloys, Naturwissenschaften. 71 (1984) 583–583. doi:10.1007/BF01189185.

[48] G.V. Raynor, V.G. Rivlin, Phase equilibria in iron ternary alloys : a critical assessment of the experimental literature / G.V. Raynor and V.G. Rivlin., Institute of Metals, London, 1988.

[49] M. Morinaga, N. Yukawa, H. Adachi, H. Ezaki, New PHACOMP and its applications to alloy design, in: Superalloys, 1984: pp. 523–532. https://www.tms.org/Superalloys/10.7449/1984/Superalloys_1984_523_532.pdf.

[50] S. Guo, C. Ng, J. Lu, C.T. Liu, Effect of valence electron concentration on stability of fcc or bcc phase in high entropy alloys, in: J. Appl. Phys., 2011: pp. 0–5. doi:10.1063/1.3587228.

[51] M.-H. Tsai, K.-Y. Tsai, C.-W. Tsai, C. Lee, C.-C. Juan, J.-W. Yeh, Criterion for Sigma Phase Formation in Cr- and V-Containing High-Entropy Alloys, Mater. Res. Lett. 1 (2013) 207–212. doi:10.1080/21663831.2013.831382.

[52] J. Dąbrowa, M. Zajusz, W. Kucza, G. Cieślak, K. Berent, T. Czeppe, T. Kulik, M. Danielewski, Demystifying the sluggish diffusion effect in high entropy alloys, J. Alloys Compd. 783 (2019) 193–207. doi:10.1016/j.jallcom.2018.12.300.

[53] N.A. Gokcen, The Mn-Ni (Manganese-Nickel) System, J. Phase Equilibria. 12 (1991) 313–321. doi:10.1007/BF02649919.

[54] W. Köster, H. Rittner, Aufbau und Eigenschaften der Kobalt-nickel-Mangen-Legierungen, Z. Met. 45 (1954) 639.

[55] M. Majdič, K. Fritscher, Beitrag zum System Cr-Mn-Ni: Konstitution und Oxidationsverhalten, Materwiss. Werksttech. 18 (1987) 329–336. doi:10.1002/mawe.19870181009.

[56] V.I. Goman'kov, A.I. Zaitsev, V.I. Kleinerman, Diagram of Structural States of Alloys of the System Ni-Fe-Mn, Russ. Met. 2 (1988) 196–200.

Table 1
Bulk compositions of each alloy in the homogenised condition. Elemental concentrations are given in atomic percent and the error is the standard deviation between five large area EDX scans.

Alloy	Cr	Mn	Fe	Co	Ni
$CrMnFeCo_{1.5}Ni$	18.4 ± 0.1	18.7 ± 0.1	18.1 ± 0.1	27.0 ± 0.1	17.8 ± 0.1
$CrMnFeCo_{0.5}Ni$	22.6 ± 0.1	21.7 ± 0.1	22.3 ± 0.1	11.3 ± 0.1	22.1 ± 0.1
CrMnFeNi	25.0 ± 0.3	25.3 ± 0.3	24.9 ± 0.2	-	24.8 ± 0.4

Table 2
Solidus temperatures obtained from DSC of alloys in the homogenised condition. The solidus was taken as the onset of melting during heating at 10˚C/min.

Alloy	DSC Solidus (˚C)
$CrMnFeCo_{1.5}Ni$	1295
$CrMnFeCo_{0.5}Ni$	1265
CrMnFeNi	1225

Table 3
Phase compositions of the $CrMnFeCo_{0.5}Ni$ alloy following 1000 h heat treatments at 900, 700 and 500˚C obtained by averaging of EDX point spectra. Elemental concentrations are given in at. % along with the standard deviation between measurements.

Condition	Phase / structure	Cr	Mn	Fe	Co	Ni
900℃	matrix / fcc	21.9 ± 0.5	21.7 ± 0.3	22.4 ± 0.3	11.5 ± 0.2	22.5 ± 0.5
	light ppt. / σ	45.2 ± 0.7	15.5 ± 0.3	20.2 ± 0.2	10.1 ± 0.2	9.0 ± 0.3
700℃	matrix / fcc	22.4 ± 0.4	21.7 ± 0.4	22.4 ± 0.3	11.4 ± 0.2	22.1 ± 0.1
	light ppt. / σ	45.6 ± 2.3	14.5 ± 0.9	20.6 ± 0.3	11.2 ± 0.2	8.0 ± 1.2
	dark ppt. / carbide	69.0 ± 9.3	10.5 ± 2.6	10.4 ± 2.2	4.0 ± 1.4	6.1 ± 3.1
500℃	matrix / fcc	22.5 ± 0.2	21.6 ± 0.2	22.5 ± 0.2	11.4 ± 0.2	22.0 ± 0.2

Table 4

Phase compositions of the CrMnFeNi alloy in the homogenised condition and following 1000 h heat treatments at 900, 700 and 500˚C. Average compositions were obtained from SEM-based EDX point spectra, except in the 500˚C condition where TEM-based EDX was used due to the fine precipitate size.

Condition	Phase / structure	Cr	Mn	Fe	Ni
1170℃	matrix / fcc	24.4 ± 0.2	25.5 ± 0.5	25.0 ± 0.4	25.1 ± 0.3
	dark ppt. / bcc	40.6 ± 0.6	20.4 ± 0.4	25.1 ± 0.3	13.9 ± 0.4
900℃	matrix / fcc	17.0 ± 0.3	29.3 ± 0.4	23.9 ± 0.5	29.8 ± 0.4
	dark ppt. / bcc	64.3 ± 2.4	13.0 ± 1.0	18.7 ± 0.5	4.0 ± 1.0
	light ppt. / σ	44.3 ± 0.7	18.9 ± 0.4	26.4 ± 0.3	10.5 ± 0.3
700℃	matrix / fcc	24.2 ± 0.2	26.2 ± 0.3	24.7 ± 0.2	25.0 ± 0.2
	dark ppt. / bcc	69.8 ± 5.5	12.0 ± 2.1	13.0 ± 2.0	5.2 ± 2.8
	light ppt. / σ	44.5 ± 0.8	17.3 ± 0.4	30.9 ± 0.3	7.3 ± 0.6
500℃	dark phase / $L1_0$*	2.7 ± 0.6	45.6 ± 1.1	3.8 ± 1.7	47.9 ± 2.5
	light phase / σ*	42.0 ± 1.4	10.5 ± 1.1	41.7 ± 0.7	5.7 ± 1.0

* TEM-EDX

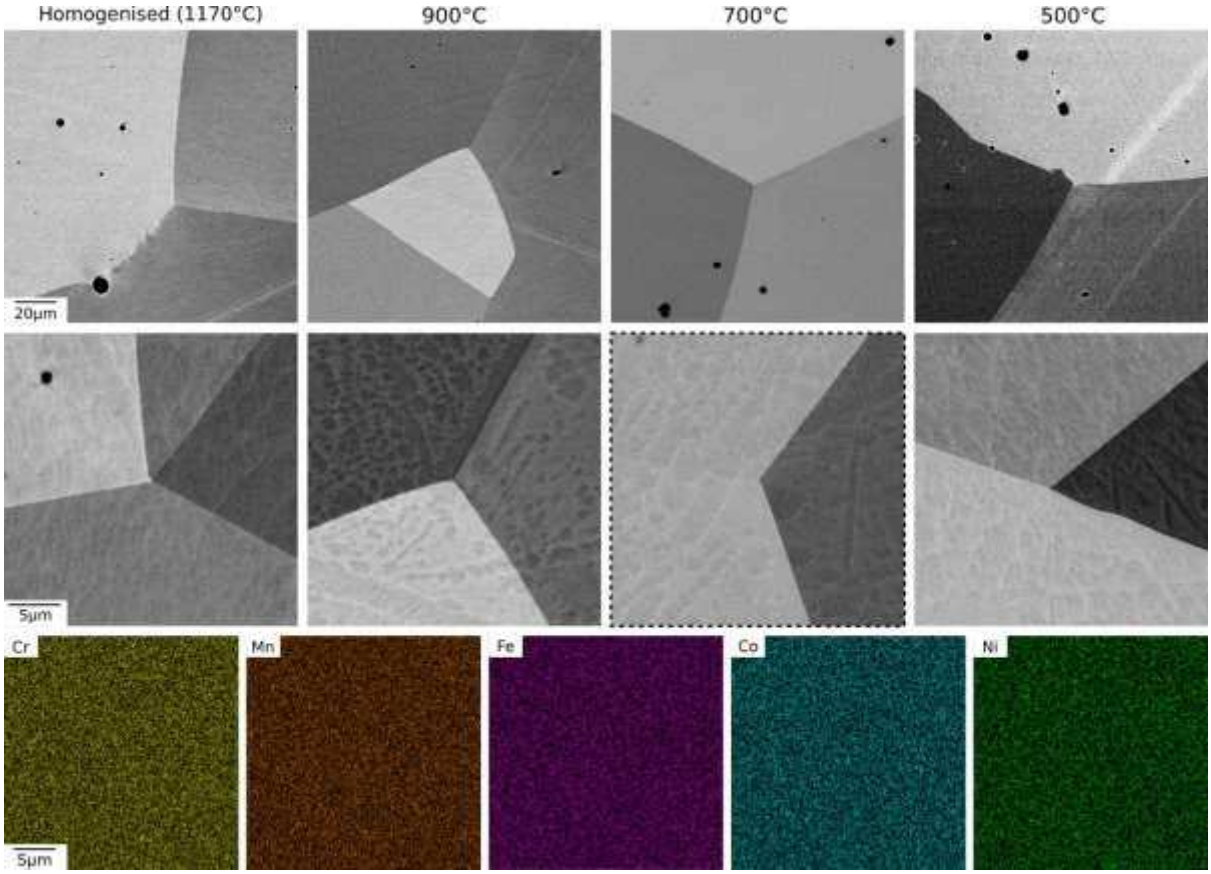

Figure 1 – BSE images of the $CrMnFeCo_{1.5}Ni$ alloy in the homogenised condition and following 1000 h heat treatments at 900, 700 and 500˚C. Representative EDX elemental partitioning maps are displayed below which correspond to the higher magnification BSE image of the 700˚C specimen (dashed outline).

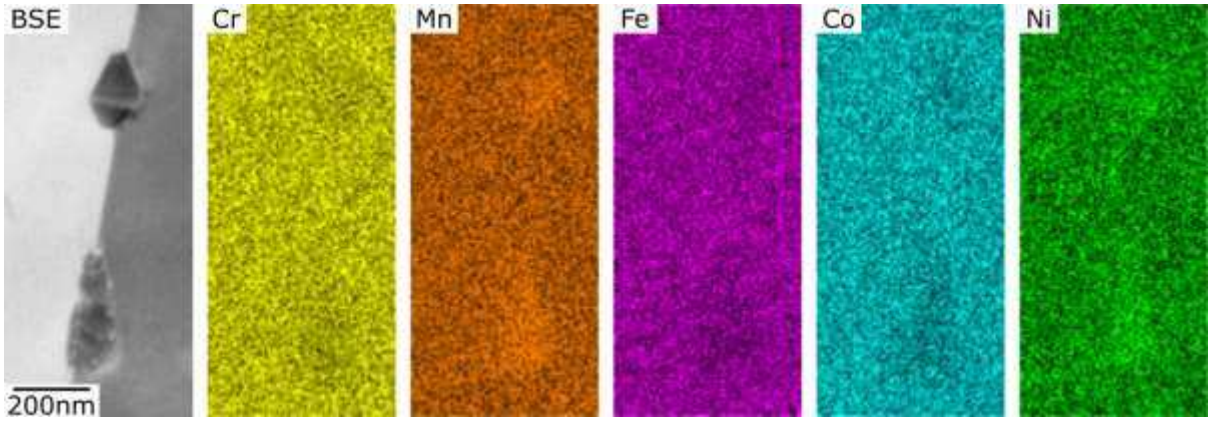

Figure 2 – BSE image and corresponding EDX elemental partitioning maps of the fine scale grain boundary precipitates observed in the $CrMnFeCo_{1.5}Ni$ alloy following a 1000 h heat treatment at 500˚C.

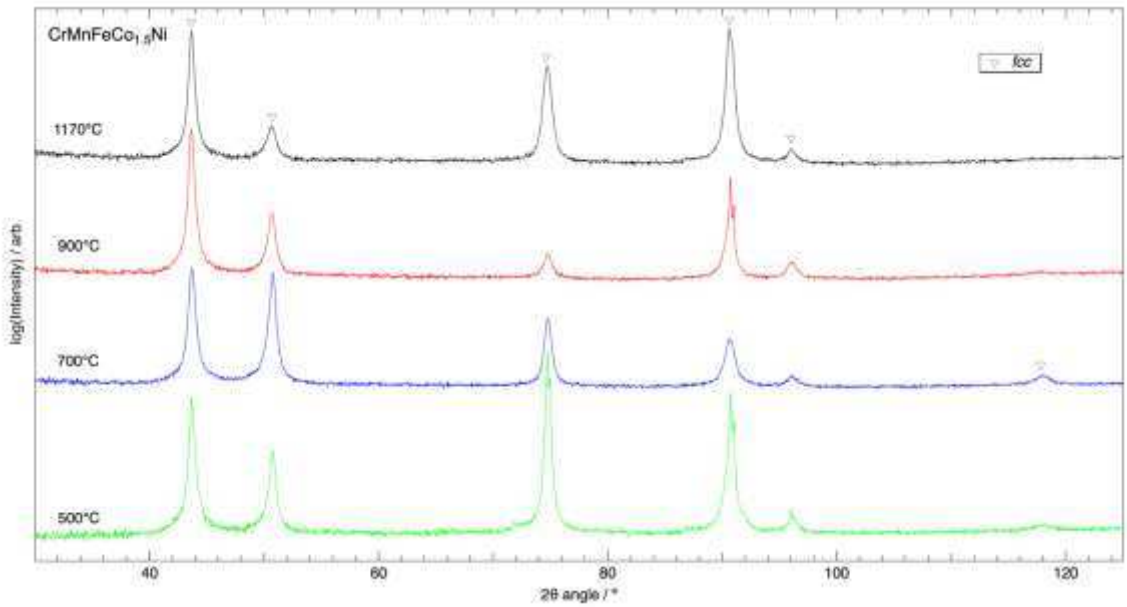

Figure 3 – XRD patterns of the $CrMnFeCo_{1.5}Ni$ alloy in the homogenised condition and following 1000 h heat treatments at 900, 700 and 500˚C.

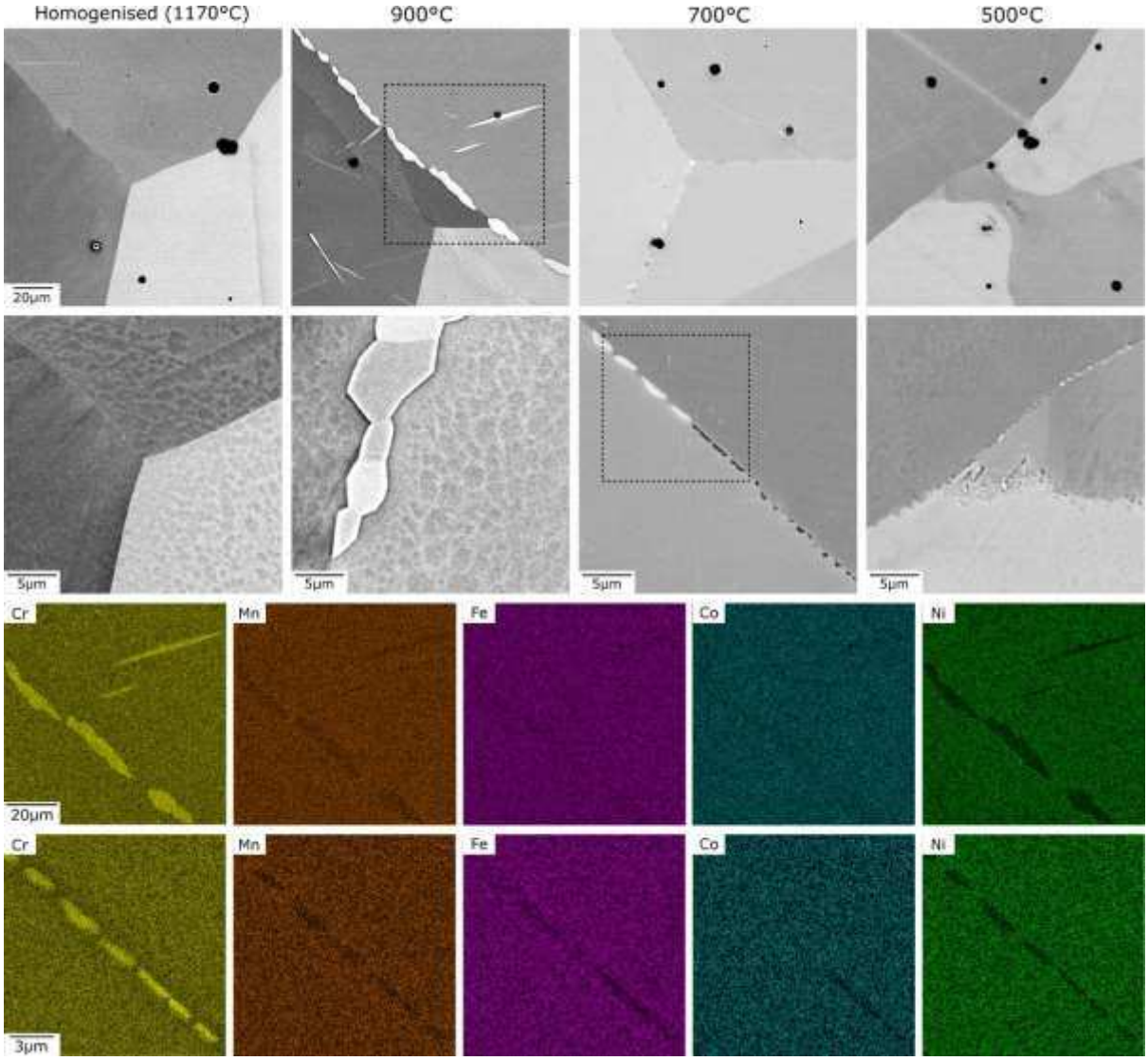

Figure 4 – BSE images of the $CrMnFeCo_{0.5}Ni$ alloy in the homogenised condition and following 1000 h heat treatments at 900, 700 and 500˚C. Representative EDX elemental partitioning maps are displayed below which correspond to regions of the BSE images indicated with a dashed outline.

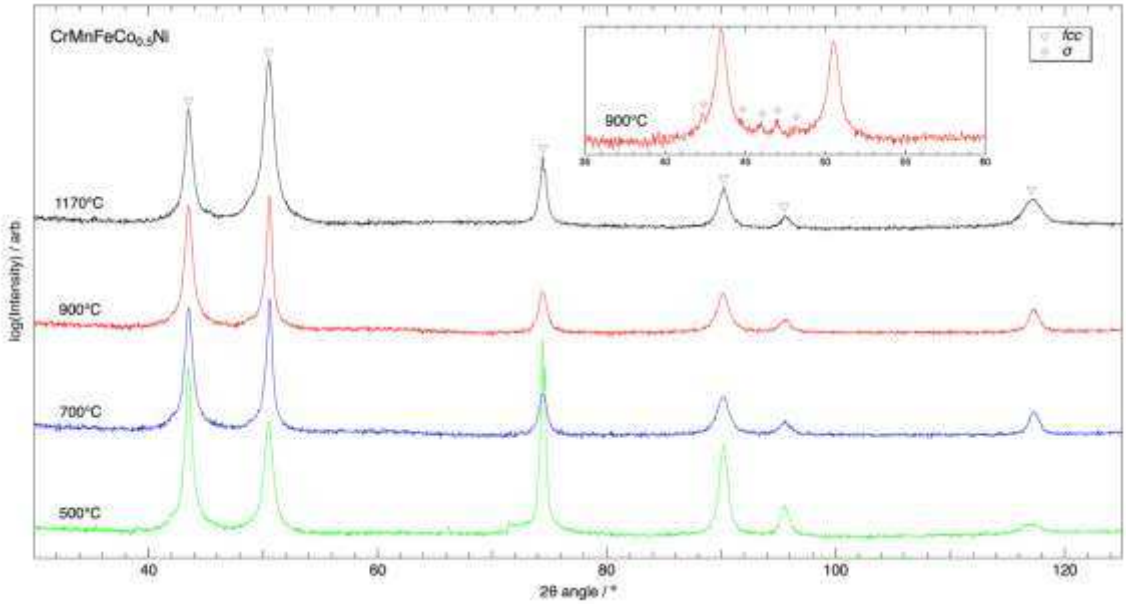

Figure 5 – XRD patterns of the $CrMnFeCo_{0.5}Ni$ alloy in the homogenised condition and following 1000 h heat treatments at 900, 700 and 500˚C. Inset shows an additional XRD pattern from a different region of the 900˚C heat-treated material in which σ reflections were identified.

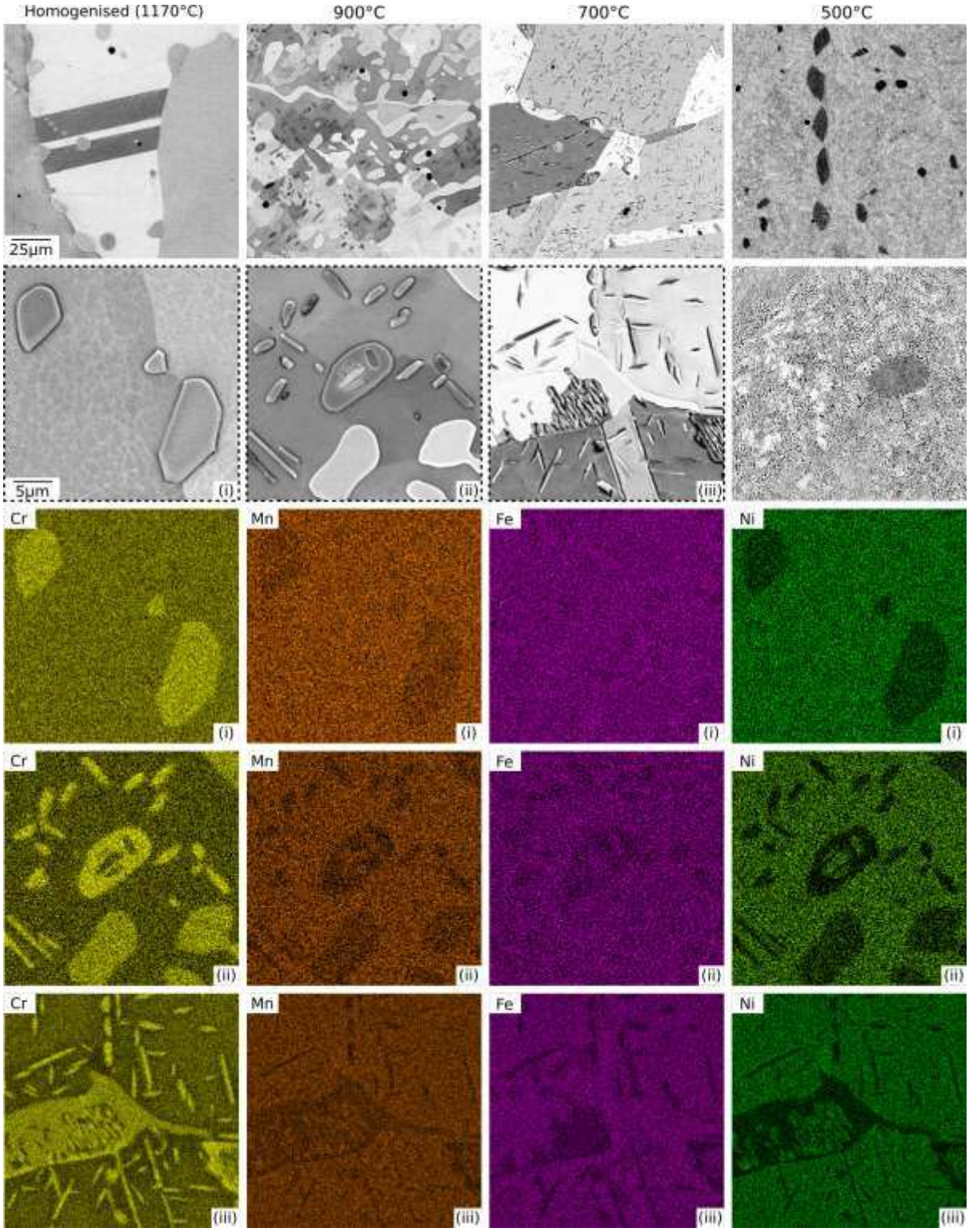

Figure 6 – BSE image of the CrMnFeNi alloy in the homogenised condition and following 1000 h heat treatments at 900, 700 and 500˚C. Representative EDX elemental partitioning maps are displayed below which correspond to the BSE images indicated with a dashed outline and labelled (i) through (iii).

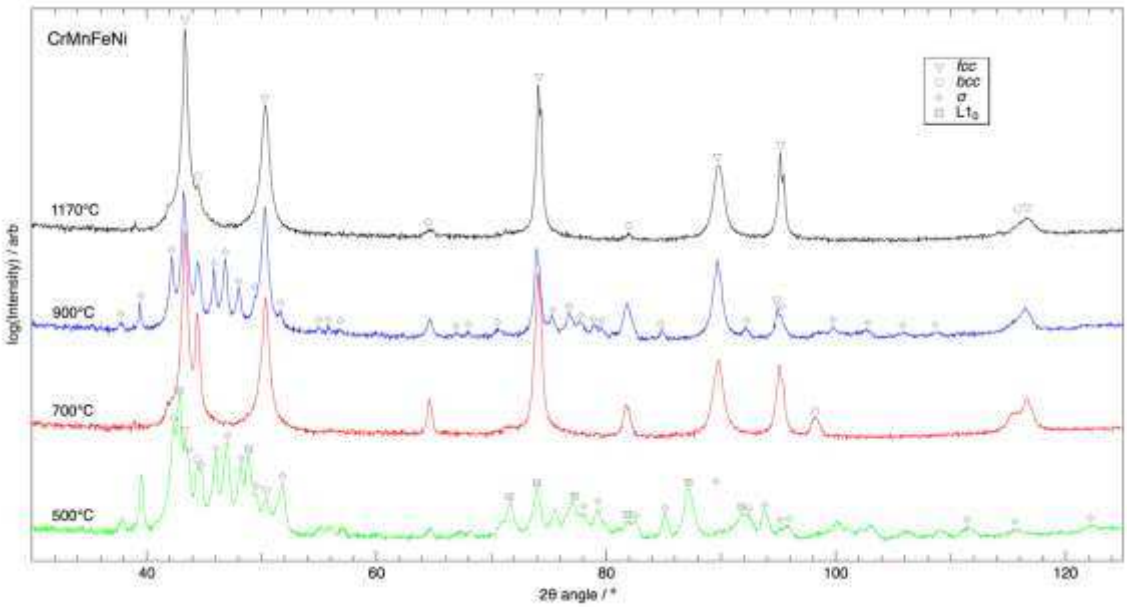

Figure 7 – XRD patterns of the CrMnFeNi alloy in the homogenised condition and following 1000 h heat treatments at 900, 700 and 500˚C.

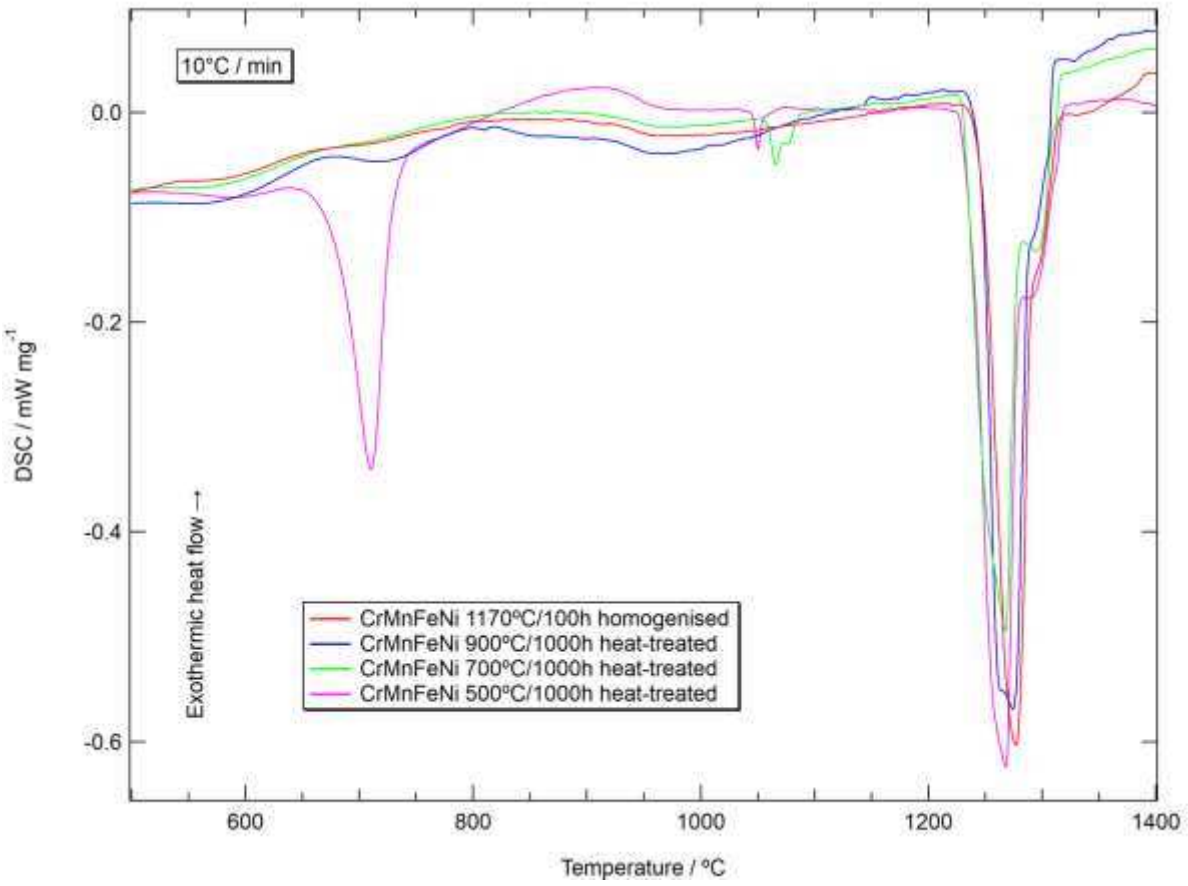

Figure 8 – Differential Scanning Calorimetry thermograms of CrMnFeNi alloy specimens upon heating. Includes material in the homogenised condition at 1170˚C for 100 h and heat-treated at 900, 700 and 500˚C for 1000 h.

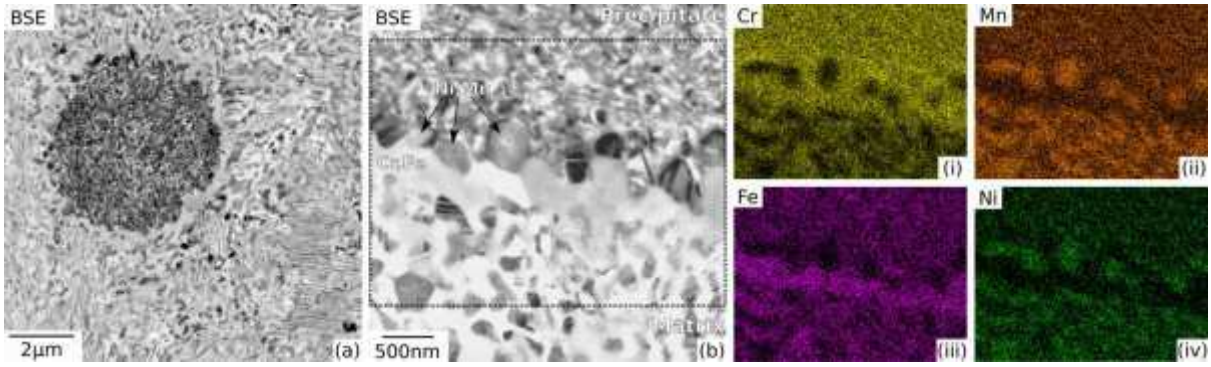

Figure 9 – (a) BSE image shows a former bcc precipitate within the former matrix of the CrMnFeNi specimen following 1000 h exposure at 500˚C. **(b)** BSE image shows the boundary between the former bcc precipitate (above) and the former matrix region (below). The EDX elemental partitioning maps, (i) through (iv), correspond to the dashed region in image (b).

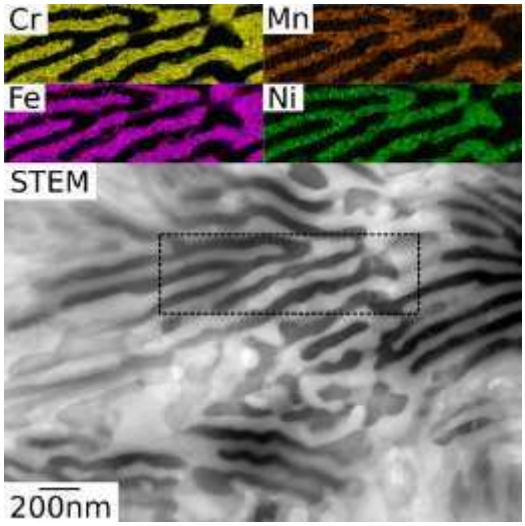

Figure 10 – STEM image of ultra-fine lamellar structures within the former matrix region of the CrMnFeCoNi specimen exposed for 1000 h at 500˚C. The EDX elemental partitioning maps above correspond to the dashed region.

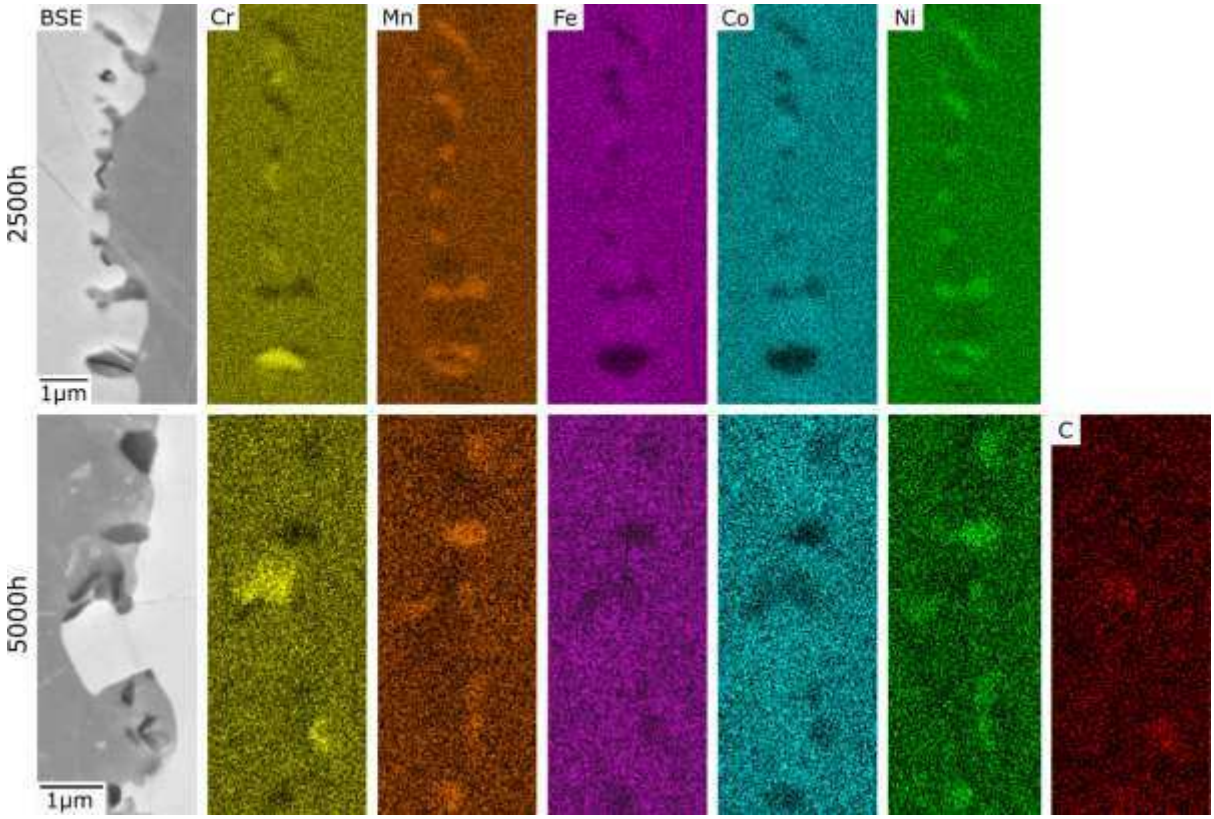

Figure 11 – BSE images and corresponding EDX elemental partitioning maps of grain boundary regions in the $CrMnFeCo_{1.5}Ni$ alloy following 2500 and 5000 h exposures at 500˚C.

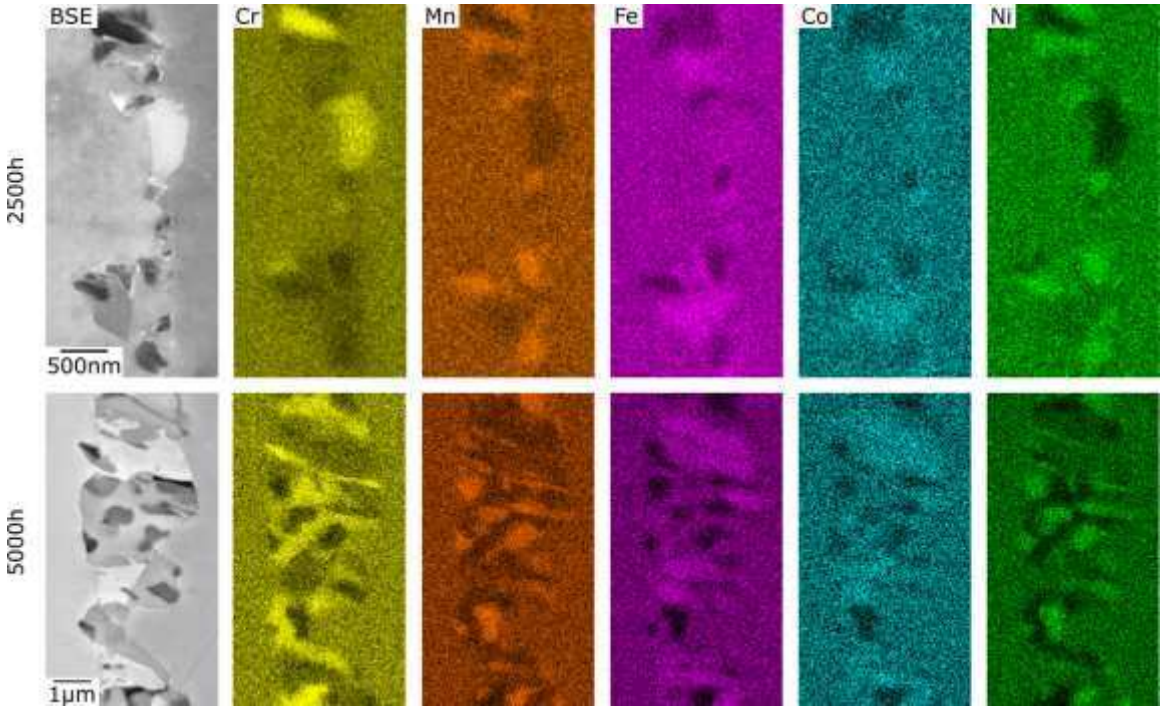

Figure 12 – BSE images and corresponding EDX elemental partitioning maps of grain boundary regions in the $CrMnFeCo_{0.5}Ni$ alloy following 2500 and 5000 h exposures at 500˚C.

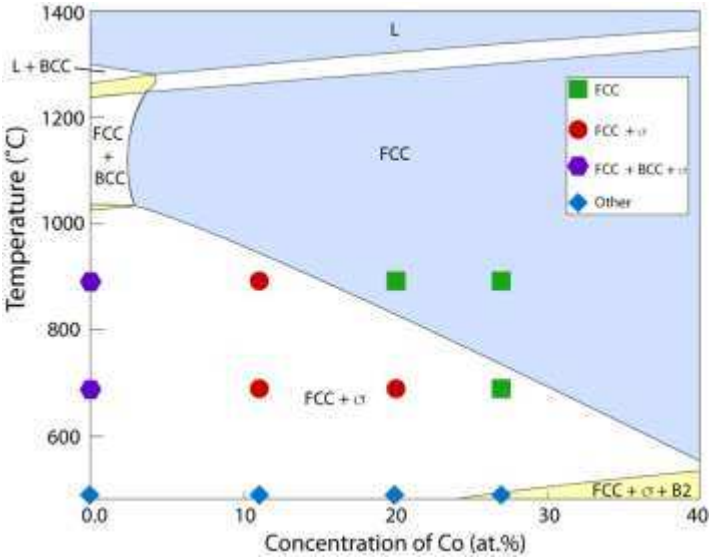

Figure 13 - Section of a Co isopleth of the $CrMnFeCo_xNi$ alloy showing the phase stability predictions of TCHEA3. Compositions and temperatures where σ phase has been experimentally observed are shown as red circles while those which were single phase fcc are denoted with green squares. Purple hexagons indicate the presence of bcc as well as σ precipitates and blue diamonds contained other phases. It should be noted that this diagram requires the data to be plotted using nominal, rather than actual, alloy compositions.